

Long-term variations in the X-ray activity of HR 1099

V. Perdelwitz¹, F. H. Navarrete², J. Zamponi², R. E. Mennickent², M. Völschow¹, J. Robrade¹, P. C. Schneider¹,
D. R. G. Schleicher², and J. H. M. M. Schmitt¹

¹ Hamburger Sternwarte, Universität Hamburg, Gojenbergsweg 112, 21029 Hamburg, Germany
e-mail: vperdelwitz@hs.uni-hamburg.de

² Departamento de Astronomía, Facultad Ciencias Físicas y Matemáticas, Universidad de Concepción, Av. Esteban Iturra s/n Barrio Universitario, Casilla 160-C, Concepción, Chile

Received 1 November 2017 / Accepted 5 June 2018

ABSTRACT

Context. Although timing variations in close binary systems have been studied for a long time, their underlying causes are still unclear. A possible explanation is the so-called Applegate mechanism, where a strong, variable magnetic field can periodically change the gravitational quadrupole moment of a stellar component, thus causing observable period changes. One of the systems exhibiting such strong orbital variations is the RS CVn binary HR 1099, whose activity cycle has been studied by various authors via photospheric and chromospheric activity indicators, resulting in contradicting periods.

Aims. We aim at independently determining the magnetic activity cycle of HR 1099 using archival X-ray data to allow for a comparison to orbital period variations.

Methods. Archival X-ray data from 80 different observations of HR 1099 acquired with 12 different X-ray facilities and covering almost four decades were used to determine X-ray fluxes in the energy range of 2–10 keV via spectral fitting and flux conversion. Via the Lomb-Scargle periodogram we analyze the resulting long-term X-ray light curve to search for periodicities.

Results. We do not detect any statistically significant periodicities within the X-ray data. An analysis of optical data of HR 1099 shows that the derivation of such periods is strongly dependent on the time coverage of available data, since the observed optical variations strongly deviate from a pure sine wave. We argue that this offers an explanation as to why other authors derive such a wide range of activity cycle periods based on optical data. We furthermore show that X-ray and optical variations are correlated in the sense that the star tends to be optically fainter when it is X-ray bright.

Conclusions. We conclude that our analysis constitutes, to our knowledge, the longest stellar X-ray activity light curve acquired to date, yet the still rather sparse sampling of the X-ray data, along with stochastic flaring activity, does not allow for the independent determination of an X-ray activity cycle.

Key words. stars: magnetic field – binaries: spectroscopic – stars: activity – stars: coroneae – X-rays: binaries

1. Introduction

Stellar activity cycles, first discovered for our Sun by Schwabe (1844), have been observed in various stars via photospheric and chromospheric activity indicators, both in single and binary systems (e.g., Berdyugina 2005; Hall et al. 2007). With the advent of space-borne X-ray observatories it has become possible to extend this research to the X-ray range, which has been shown to be a robust tracer of activity cycles (Favata et al. 2004; Robrade et al. 2012; Lalitha & Schmitt 2013; Wargelin et al. 2017).

In addition to enabling the study of the underlying dynamo, magnetic activity cycles have been suggested to be the cause of timing variations in close binary systems. These have been observed over a broad range of such systems, including Algol and RS CVn systems, with relative period modulation amplitudes of $\Delta P/P \sim 10^{-5}$ and typical cycle periods of 30–50 yrs, as well as cataclysmic variables and W UMa systems with $\Delta P/P \sim 10^{-6}$ and cycles of 5–30 yrs (e.g., Warner 1988; Hall 1989). Post-common-envelope binaries (PCEBs) exhibit a very similar behavior, with $\Delta P/P \sim 10^{-6}$ and modulation periods of 10–30 yrs (Zorotovic & Schreiber 2013; Bours et al. 2016).

A simple explanation of these period variations is to invoke the presence of a third body, giving rise to the variation via the

light travel effect (LTE) effect (see e.g., Pribulla et al. 2012). However, while the existence of such circumbinary companions has been postulated to explain timing variations in various systems, to date none of them has been confirmed with an independent method; for example, the third body causing timing variations in V471 Tau first proposed by Beavers et al. (1986) could not be confirmed with a direct imaging attempt with VLT-SPHERE (Hardy et al. 2015).

It is therefore essential to assess whether other mechanisms can produce the observed period variations. Such a mechanism could be a powerful magnetic activity cycle as expected in the presence of rapidly rotating and convective stars (Baliunas et al. 1996). During the course of a cycle, the stellar angular momentum could be redistributed, thus leading to quasi-periodic changes of the stellar quadrupole moment and orbital period. This model, originally proposed by Applegate (1992), has been improved by Lanza & Rodonò (1999) by adopting a consistent formulation for virial equilibrium. Brinkworth et al. (2006) extended the model by introducing a finite-shell formalism, showing that the latter substantially increases the energy required to drive the Applegate mechanism. Völschow et al. (2016) applied this model to a total of 16 close binary systems and showed that the mechanism is clearly feasible in four of the systems, while it can be ruled out on energetic grounds in

eight cases; an additional amount of four systems remained unclear. Further, improved models for the Applegate mechanism have been put forward by Lanza (2005, 2006). The authors found that if the observed period variations were driven by the Applegate mechanism, the energy dissipation in the convection zone would exceed the star's luminosity. As shown recently, the resulting changes of the quadrupole moment may also affect the mass transfer rate between the stars, and potentially give rise to the long cycles in Double Periodic Variables (Schleicher & Mennickent 2017).

One of the systems exhibiting substantial period variations is HR 1099 (or V711 Tau), a RS CVn binary of spectral type K1 IV+G5 V with an orbital period of 2.84 days first identified by Bopp & Fekel (1976). Its proximity of 30.7 pc (van Leeuwen 2007) and its very high level of magnetic activity in all available indicators have made it one of the prime candidates for the study of stellar dynamos (see e.g., Donati 1999, García-Alvarez et al. 2002, Osten et al. 2004 and Cao & Gu 2015). Several authors have searched for magnetic activity periods in HR 1099 via long-term photometry, which is sensitive to detecting variations in the spot coverage. Such activity cycles have been reported by Lanza et al. (2006), who obtain a 19.5 ± 2 yr period, by Berdyugina & Henry (2007), who derive a period of 15–16 yr, and by Muneer et al. (2010) who report a 14.1 ± 0.3 yr period. An inspection of the light curves shows clear periodicities despite a very large scatter in the optical photometry. In addition to their activity period derivation, Muneer et al. (2010) show that the O–C diagram of HR 1099 can be improved considerably by fitting the orbital period of the system to the O–C data, resulting in a well-defined sinusoidal shape with a period of 36.3 ± 1.9 yrs.

As a consequence, the question arises whether magnetic activity is also periodic in other proxy indicators. Drake et al. (2014) have carried out study into the long-term X-ray variability of AR Lac found that it is constant and displays no signs of a coronal activity cycle. In this paper we therefore independently investigate the magnetic activity period of HR 1099 using an X-ray light curve spanning almost 40 yrs in order to test whether this method is a valid means to test the Applegate mechanism. A theoretical motivation is given in Sect. 2 and the observational data are described in Sect. 3. A summary and discussion of our results is given in Sect. 4.

2. Theoretical motivation

We show in the following that a long-term magnetic activity cycle can be qualitatively understood through simple dynamo models. For this purpose, we employ the relation between rotation period and activity cycle given as (Soon et al. 1993; Baliunas et al. 1996)

$$P_{\text{cycle}} = D^\alpha P_{\text{rotation}}, \quad (1)$$

where D is the dynamo number and α is a parameter of order 0.5. Furthermore, D is related to the Rossby number, Ro , via

$$D = Ro^{-2} \quad (2)$$

with $Ro \propto P/\tau$, where P is the period and τ is the convective turnover time, can also be obtained from (Soker 2000)

$$Ro = 9 \left(\frac{v_c}{10 \text{ km s}^{-1}} \right) \left(\frac{H_p}{40 R_\odot} \right)^{-1} \left(\frac{\omega}{0.1 \omega_{\text{Kep}}} \right)^{-1} \left(\frac{P_{\text{Kep}}}{1 \text{ yr}} \right), \quad (3)$$

with v_c denoting the convective velocity, H_p the pressure scale height, and ω , ω_{Kep} , and P_{Kep} the angular velocity, Keplerian

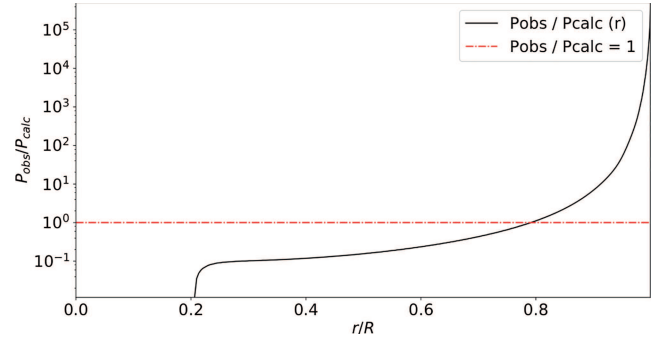


Fig. 1. Radial profile of $P_{\text{obs}}/P_{\text{calc}}$ obtained from Eq. (1) (black curve) and $P_{\text{obs}}/P_{\text{calc}} = 1$ (horizontal red line). The lines meet at $r/R \sim 0.8$, suggesting that the observed activity cycle is driven in this region.

angular velocity, and Keplerian orbital period, respectively. The convective velocity and the pressure scale height are properties inside the star, which we calculate using the stellar evolution code MESA (Paxton et al. 2011). We first evolve a Sun-like star with solar-like rotation up to 4.7 Gyr, which we use to calibrate α in Eq. (1). The model employs a solar metallicity, and we choose mixing length theory MLT = ‘ML1’ with $\alpha_{\text{MLT}} = 1.5$. Considering that the solar dynamo is expected to take place at the bottom of the convection zone with $R \sim 0.7 R_\odot$, we use the properties at that point and find that $\alpha \sim 0.86$. We subsequently run a simulation for the subgiant in HR 1099 assuming that it is tidally locked, so that its rotation corresponds to a fixed fraction of the critical angular velocity with $\Omega_{\text{ZAMS}}/\Omega_{\text{crit}} = 0.28$ following from the binary rotation period¹. The mass of the subgiant is set to $M = 1.3 M_\odot$ based on Bopp & Fekel (1976). The run is stopped when the radius is $R = 4.0 R_\odot$. We calculate the dynamo number D as a function of radius from the convection velocity v_c and the pressure scale height H_p , allowing us to compute the expected dynamo activity cycle as a function of radius. In Fig. 1, the black curve shows the fraction $P_{\text{obs}}/P_{\text{calc}}$ as a function of the radial coordinate r/R and the horizontal red line is $P_{\text{obs}}/P_{\text{calc}} = 1$, where P_{obs} is assumed here to be of the order of 20 yrs. They intersect at $r/R \sim 0.8$.

While based on simplifying assumptions, the result suggests that a dynamo cycle of ~ 20 yrs would be predominantly driven in the outer parts of the shell. We further make a preliminary assessment if such a dynamo cycle may be responsible for the O–C variations observed in the system through the Applegate mechanism. As a remark, we note that the ratio between activity cycle and O–C variation cycle is approximately 1:2, as is the case in previously observed systems (e.g., Lanza et al. 2001). The expected ratio is however not well explored in theoretical models. To assess whether the Applegate mechanism is energetically feasible, we employ the formalism developed by Völschow et al. (2016) using the two-zone model, which has been implemented in a publicly available Applegate calculator². In this calculation, we neglect the mass contribution from the radiative core, where dynamo effects and related changes of the angular momentum cannot be expected to be relevant (see also discussion in Lanza 2006). We first recalculate the k_1 and k_2 coefficients defined by Völschow et al. (2016) based on the MESA output neglecting the central core. The lowest energy is found when we consider the exchange of angular momentum between the shells with $0.2 < r/R_{\text{in}} < 0.65$ and $0.65 < r/R_{\text{out}} < 1$. The result suggests

¹ Here, we use the notation of Paxton et al. (2013).

² <http://theory-starformation-group.cl/applegate/>

that the Applegate mechanism may be energetically feasible, and would be driven somewhat more in the interior of the star.

3. Observations

HR 1099 is one of the brightest known coronal X-ray sources. Therefore HR 1099 has been observed – starting in 1978 – by virtually all X-ray facilities, even those with small effective areas and lower sensitivity, thus forty years of X-ray observations are available. Specifically, we have identified a total of 78 data sets, 60 in the form of spectra and 18 as count rates, from 12 different facilities. Many of these observations have been carried out for calibration purposes or with the goal of studying stellar flares (Kashyap & Drake 1999; Brinkman et al. 2001; Osten et al. 2004; Tsuboi et al. 2016), yet, to our knowledge, no long-term activity study of HR 1099 based on several data sets has been carried out so far. In Table 1 we provide a detailed list of these X-ray observations with the appropriate references.

For the derivation we have to distinguish between two types of data, namely (i) spectra and (ii) data without spectral information, which we converted into fluxes assuming a model based on *XMM-Newton* spectra.

3.1. Spectral data

The majority of the spectral X-ray data of HR 1099 are available as spectral pipeline products from the NASA HEASARC³ data base; we used the HEASARC data whenever available. Specifically, we custom processed the *XMM-Newton* data (acquired from the ESA archive) with the Science Analysis System (Gabriel et al. 2004) and downloaded *Chandra* spectra from the TGCat database (Huenemoerder et al. 2011). MAXI data were obtained via the on demand tool on the project website⁴, with a binning of 2 yrs due to the small effective area of the instrument and target and background apertures of 2 and 3 deg. *Swift* data were generated with the Build *Swift*-XRT products tool (Evans et al. 2009) on the *Swift* homepage⁵.

For the following spectral analysis we used XSPEC version 12.7.1 (Arnaud 1996). The 60 spectra were grouped with the grppha task to a minimum of 15 cts per spectral bin and clipped to the range of 2–10 keV, a spectral range covered by all but one instrument, the *Einstein* SSS. Due to an erroneous normalization of the pipeline products of the *Einstein* SSS and MPC, it was not possible to fit spectra from both instruments simultaneously and thereby cover the entire wavelength range. This and the presence of an instrumental artifact at ≈ 3.5 keV led us to utilize only the SSS data and extrapolate the spectra beyond 3 keV by using the XSPEC energies and adding 100 additional linear bins up to 10 keV.

The first spectral fit was performed with a cflux*(mekal + mekal) model, where the model abundances were linked to each other, leaving six free parameters: flux, kT_1 , $norm_1$, kT_2 , $norm_2$ and abundance. All spectra with a reduced $\chi^2 > 2$ were then refitted after adding a third mekal component to the model. We were merely interested in obtaining a good flux estimate in the energy range in question, and not in any coronal parameters such as plasma temperatures or abundances. For the majority of the spectra our fits yielded a reduced χ^2 in the range of 0.63–1.8 (see Table 1), the exceptions being one *Einstein* SSS and two RXTE spectra.

³ heasarc.gsfc.nasa.gov

⁴ maxi.riken.jp

⁵ swift.ac.uk

Table 1. Instruments in use.

Mission	Instrument	Energy range (keV)	References	#
HEAO1 <i>Einstein</i>	A2	2–60	[1]	5
	IPC	0.4–4	[2]	4
	SSS	0.5–4.5		4
EXOSAT	ME	1–50	[3]	8
ROSAT	PSPC	0.08–2.9	[4]	2
	HRI	0.1–2.4		9
Ginga	LAC	1.5–37	[5]	3
ASCA	SIS0,1	0.3–12	[6]	2
	GIS2,3	0.4–12		2
RXTE	PCA	1.4–100	[7]	17
<i>BeppoSAX</i>	LECS	0.1–14	[8]	1
	MECS	0.8–12		1
<i>XMM-Newton</i>	EPIC PN	0.1–12	[9]	8
	MOS1	0.1–12		1
<i>Chandra</i>	HETG,ACIS-S	0.4–8	[10]	2
<i>Swift</i>	XRT	0.2–10	[11]	9
MAXI	GSC	2–20	[12]	4
	SSC	0.7–7		4

Notes. The last column shows the total number of spectra analyzed in this work. For some instruments spectra from multi-instrument missions were fitted simultaneously (see Sect. 3.1).

Instrument references. Rothschild et al. (1979) [1]; Giacconi et al. (1979) [2]; Taylor et al. (1981) [3]; Truemper (1982) [4]; Turner et al. (1989) [5]; Tanaka et al. (1994) [6]; Jahoda et al. (1996) [7]; Boella et al. (1997) [8]; Jansen et al. (2001) [9]; Weisskopf et al. (2002), Canizares et al. (2005) [10]; Gehrels et al. (2004) [11]; Matsuoka et al. (2009) [12].

The output fluxes from the XSPEC cflux model were used for further analysis along with flux uncertainties obtained with the XSPEC error function for a 90% confidence level.

In the case of multi-instrument missions with more than one instrument covering 2–10 keV, all spectra were fitted simultaneously, with the exception of the photon-starved *BeppoSAX* data, where a simultaneous fit yielded a reduced $\chi^2 > 3$.

3.2. Flux conversion

We converted the 18 data sets from those instruments, for which only count rates were available (ROSAT, *Einstein* IPC, Ginga) into physical fluxes by computing conversion factors in the following manner. Two *XMM-Newton* spectra were fitted with a 3-T apec model in the spectral range 0.2–12.0 keV, one with a medium flux level as determined in the analysis described in the previous Section (Obs.-ID 0116890901), and one with the lowest flux of the entire *XMM-Newton* data set (Obs.-ID 0116200701). After the first fit, the plasma temperatures and abundances were frozen to the closest value available in the HEASARC WebPIMMS tool, after which the fit is repeated. The determined plasma temperatures and relative emission measures, along with the model component normalizations, were used as input for WebPIMMS, and a conversion factor was determined for all instruments in question. The conversion factors derived via the *XMM-Newton* Obs.-ID 0116890901 were then used to convert instrument count rates into physical fluxes, while the difference between the mid- and low-state conversion factors was used as a systematic error. The inclusion of this systematic error was necessary due to the fact that a flux conversion without any a priori knowledge of the coronal properties during a given

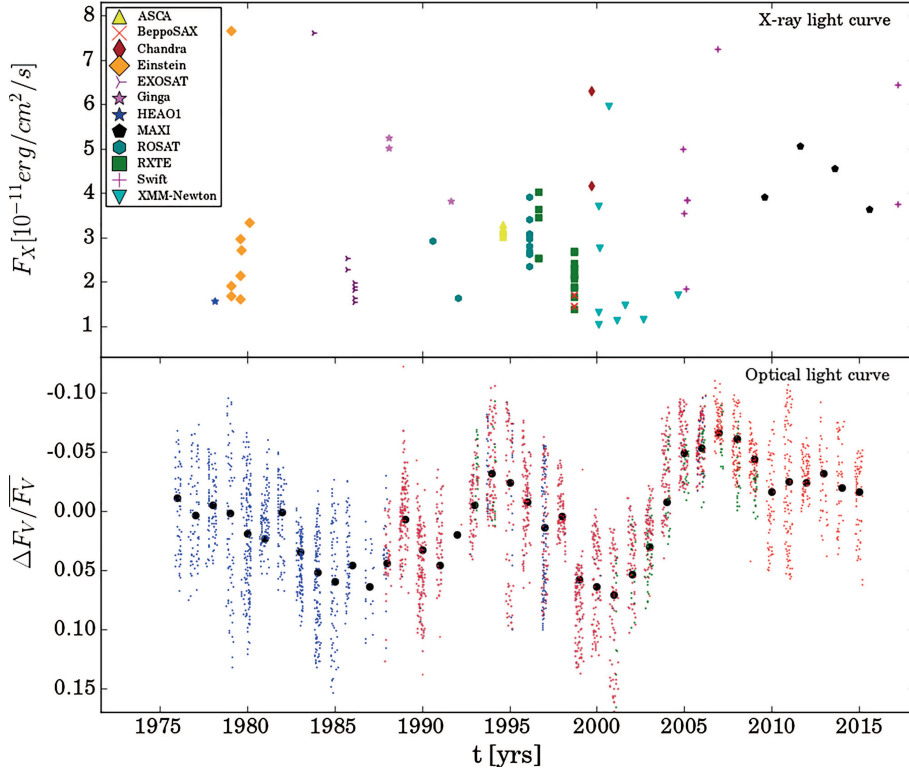


Fig. 2. Light curves of HR 1099 in the X-ray and optical regime. *Top panel:* X-ray flux of HR 1099 in the energy range 2–10 keV as a function of time. For clarity, we omitted the error bars in this plot, but the values can be found in Table 1. *Bottom panel:* change in optical flux (V-band) as a function of time. Blue data are taken from Berdyugina & Henry (2007), green data from Muneer et al. (2010) and red data from Jetsu et al. (2017). The black dots represent an annual binning of the data.

observation must consider the entire range of system parameters representative of the system. All conversion factors are displayed in Table 1 along with the other data.

3.3. Light curve analysis

3.3.1. Period analysis

In this Section we analyze possible periodicities in the X-ray data alone. The resulting X-ray light curve comprising of 80 observations is displayed in the top panel of Fig. 2.

We excluded the *Swift* exposure ID 582894000 from further analysis on the grounds that the derived flux is two orders of magnitude larger compared to the rest of the data; this data set is the only *Swift* observation of the target connected to a TDRSS message, and therefore was likely triggered by an extreme flare of the system.

The remaining 79 data points were analyzed with the generalized Lomb-Scargle algorithm included in the PyAstronomy package with a normalization following Zechmeister & Kürster (2009) while weighting each observation with the determined flux error; the upper left panel of Fig. 3 shows the resulting periodogram. In order to assess the significance derived via the Lomb-Scargle periodogram, we ran a bootstrap approach with 10^4 repetitions where, in every repetition, the fluxes were randomly drawn with replacement and distributed to the observation epochs. The FAP is then the ratio between all repetitions with a higher LS power than that of the unperturbed analysis and the total number of repetitions. In the top left panel Fig. 3 we marked the FAP levels of 50 and 80% as dashed blue lines, and in the top right panel the maximum period distribution of all repetitions is displayed as a histogram. While the periodogram exhibits a peak at $P = 21.2$ yrs, the false alarm probability is higher than 50%, indicating that no significant period could be detected. A folded light curve assuming the putative period of 21.2 yrs (Fig. 4) confirms this finding, that is, at any given phase the entire range of fluxes is covered.

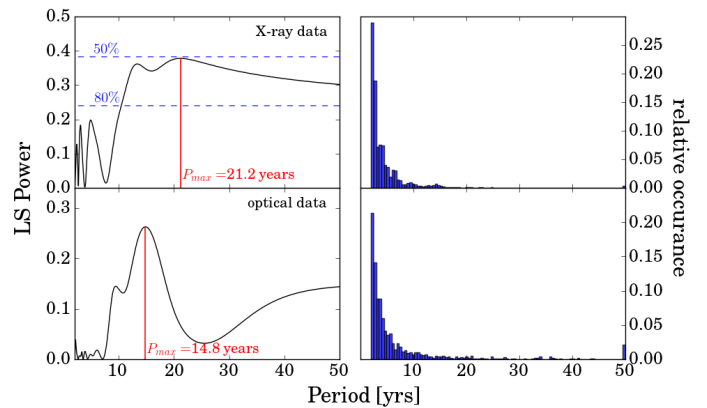


Fig. 3. Lomb-Scargle periodograms and distribution of periods in the bootstrap approach of the X-ray and optical data. *Upper left panel:* Lomb-Scargle periodogram of the X-ray data. The FAP levels of 50 and 80% resulting from the bootstrap analysis described in Sect. 3.3 are marked as blue lines. *Upper right panel:* distribution of maximum periods determined for all 10^4 repetitions. *Lower panels:* results of a similar analysis of the optical data. No FAP levels are displayed here, since none of the bootstrap repetitions yielded a higher Lomb-Scargle power than the unperturbed data.

In order to check the influence of flaring events on the period analysis, we checked all available light curves for flares, and identified 33 observations without obvious large flaring events (see last column of Table 1). However, a period analysis of this reduced data set yielded no significant period, most likely due to insufficient temporal coverage.

3.3.2. Comparison to optical data

We performed a Lomb-Scargle analysis similar to the one described in Sect. 3.3 on an optical data set comprising of archival

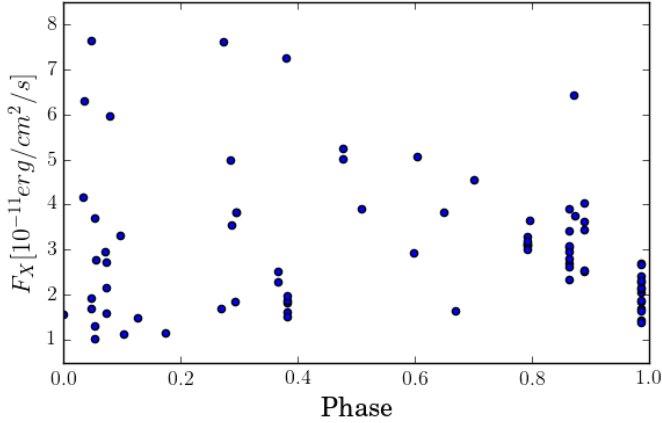


Fig. 4. Folded X-ray light curve under the assumption of the 21.2 yr period determined in the LS analysis.

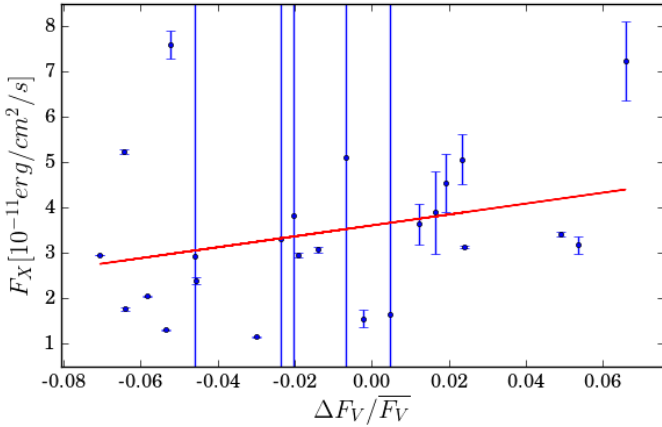


Fig. 5. Correlation between the optical and X-ray light curve. The best fit linear curve is marked with a red line.

data provided by [Berdyugina & Henry \(2007\)](#), [Muneer et al. \(2010\)](#) and [Jetsu et al. \(2017\)](#). The resulting periodogram and distribution of periods in the bootstrap approach is displayed in the lower panels of Fig. 3. Since none of the 10^4 repetitions yielded a higher LS power than the maximum-likelihood period of 14.8 yrs, no FAP could be determined, but rather an upper limit of 0.01%.

We tested the correlation between optical and X-ray data by binning each data set into bins of one year and then performed a cross-correlation between the two. The data yielded only a marginal correlation (see Fig. 5) with a Pearson coefficient of 0.29. Computing a periodogram for different sets of archival optical data, starting with a window of ten years from the first data set and sequentially adding a year of data, we can show the effects of temporal coverage on derived periods. Fig. 6 shows the complete photometric light curve (top panel), as well as the period of maximum Lomb-Scargle power as a function of the upper limit of the time window. While the analysis of a sinusoidal data set with this method should result in near-constant values, we observe a large spread in the derived periods, which clearly depend on the time coverage of available data (as also evidenced by the previously mentioned disagreement between other authors).

4. Discussion and conclusions

Our study of the longterm X-ray evolution of the active RS CVn binary HR 1099 has produced the first X-ray light curve of the

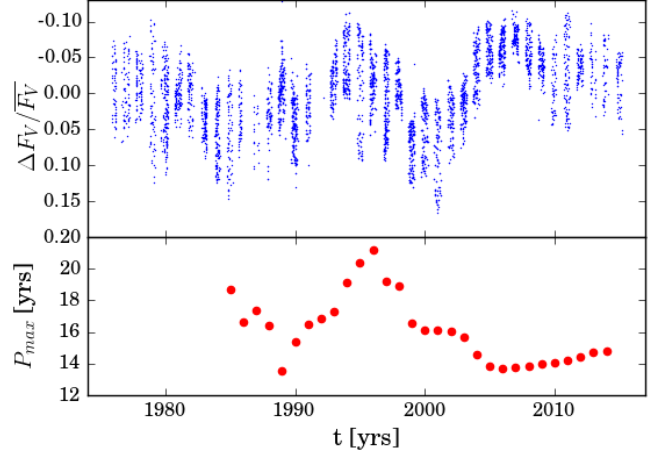


Fig. 6. Dependence of the maximum-likelihood period on temporal coverage of available data. *Top:* photometric light curve in V-band. *Bottom:* maximum periods derived via Lomb-Scargle analysis for data sets with increasing temporal coverage. The x -value of each point is the upper limit of the analyzed time window. The range of derived periods has a strong dependence on the time window.

system spanning several decades. We stress that most data used for this work are available as standard pipeline products.

We must nevertheless add some caveats: The X-ray instrumentation used substantially differs, some of the instruments are imaging, others are non-imaging, some instruments offer high spectral resolution, others none and the covered spectral bands differ. Some instruments cover only the energy band above 2 keV (such as RXTE or MAXI); for those instruments HR 1099 appears as a “soft” stellar source and the derived fluxes depend sensitively on the temperatures used. Other instruments, such as *XMM-Newton* cover the whole band pass, yet others, like the ROSAT PSPC have little to no sensitivity at energies above 2 keV and therefore the flux needs to be extrapolated, which again depends on the spectral model used. We argue that our choices for the flux conversion are reasonable, however, we also admit that they are likely affected by systematic uncertainties that are beyond our control such as the strength of the soft component during the RXTE observations and the strength of the hard component during the ROSAT observations.

Only a marginal correlation between the optical and X-ray data could be determined and we could not detect any significant periodicity in the X-ray data. Furthermore, the bootstrap method applied to estimate the FAP only accounts for white noise, and an approach including red noise would further decrease the significance of the detected peak ([Vaughan 2005](#); [VanderPlas 2018](#)). One possible explanation for the large FAP is the substantial scatter within the light curve, which is most likely dominated by stochastic X-ray flaring activity.

Another likely contributor is the shape of the activity modulation itself. Even when taking into account that the peak in the Lomb-Scargle periodograms of both X-ray and optical data is broad, indicating an error ≥ 5 yrs, the maximum-likelihood periods are only in partial agreement with the photometric cycles derived by other authors, namely [Lanza et al. \(2006; 19.5 ± 2 yrs\)](#), [Berdyugina & Henry \(2007; 15 – 16 yrs\)](#) and [Muneer et al. \(2010; 14.1 ± 0.3 yrs\)](#), as well as our own analysis of the complete data set (14.8 yrs). We thus conclude that the activity cycle of HR 1099 is more complicated than a simple sinusoidal, and we could only determine a characteristic timescale of 14.8 yrs based on the optical data.

Lanza et al. (2006) claim a correlation of the magnetic cycle of HR 1099 with the orbital period variations, arguing that the orbital period variations display a period twice as long as that of the activity cycle, hinting at the Applegate mechanism. Muneer et al. (2010) do, in fact, determine the period variations to be 36.3 ± 1.9 yr. However, in order to test this hypothesis, a continued long-term monitoring of HR 1099 and related objects using multiple activity indicators is required.

Acknowledgements. VP acknowledges funding through the DLR and DFG. VP, DRGS, FHN and JAZF thank for funding through Fondecyt regular (project code 1161247). DRGS is grateful for funding through the “Concurso Proyectos Internacionales de Investigación, Convocatoria 2015” (project code PII20150171) and ALMA-Conicyt (project code 31160001). REM acknowledges funding via VRID-ENLACE 214.016.002-1.0 and VRID-ENLACE 218.016.004-1.0. DRGS, FHN and REM further thank for funding through the BASAL Centro de Astrofísica y Tecnologías Afines (CATA) PFB-06/2007. This research has made extensive use of data and/or software provided by the High Energy Astrophysics Science Archive Research Center (HEASARC), which is a service of the Astrophysics Science Division at NASA/GSFC and the High Energy Astrophysics Division of the Smithsonian Astrophysical Observatory. This research has made use of MAXI data provided by RIKEN, JAXA and the MAXI team. It is partly based on observations obtained with *XMM-Newton*, an ESA science mission with instruments and contributions directly funded by ESA Member States and NASA. The scientific results reported in this article are based in part on data obtained from the *Chandra* Data Archive. This work made use of data supplied by the UK *Swift* Science Data Centre at the University of Leicester. We would like to thank Steve Drake, Michael Corcoran and Bryan Irby (HEASARC) for help with the *Einstein* data set.

References

- Applegate, J. H. 1992, *ApJ*, **385**, 621
- Arnaud, K. A. 1996, in *Astronomical Data Analysis Software and Systems V*, ed. G. H. Jacoby, & J. Barnes, *Astronomical Society of the Pacific Conference Series*, **101**, 17
- Baliunas, S. L., Nesme-Ribes, E., Sokoloff, D., & Soon, W. H. 1996, *ApJ*, **460**, 848
- Beavers, W. I., Lui, A., & Herczeg, T. J. 1986, *ApJ*, **300**, 785
- Berdyugina, S. V. 2005, *Liv. Rev. Sol. Phys.*, **2**, 8
- Berdyugina, S. V., & Henry, G. W. 2007, *ApJ*, **659**, L157
- Boella, G., Butler, R. C., Perola, G. C., et al. 1997, *A&AS*, **122**, 199
- Bopp, B. W., & Fekel, Jr., F. 1976, *AJ*, **81**, 771
- Bours, M. C. P., Marsh, T. R., Parsons, S. G., et al. 2016, *MNRAS*, **460**, 3873
- Brinkman, A. C., Behar, E., Güdel, M., et al. 2001, *A&A*, **365**, L324
- Brinkworth, C. S., Marsh, T. R., Dhillon, V. S., & Knigge, C. 2006, *MNRAS*, **365**, 287
- Canizares, C. R., Davis, J. E., Dewey, D., et al. 2005, *PASP*, **117**, 1144
- Cao, D., & Gu, S. 2015, *MNRAS*, **449**, 1380
- Donati, J.-F. 1999, *MNRAS*, **302**, 457
- Drake, J. J., Ratzlaff, P., Kashyap, V., et al. 2014, *ApJ*, **783**, 2
- Evans, P. A., Beardmore, A. P., Page, K. L., et al. 2009, *MNRAS*, **397**, 1177
- Favata, F., Micela, G., Baliunas, S. L., et al. 2004, *A&A*, **418**, L13
- Gabriel, C., Denby, M., Fyfe, D. J., et al. 2004, in *Astronomical Data Analysis Software and Systems (ADASS) XIII*, ed. F. Ochsenbein, M. G. Allen, & D. Egret, *Astronomical Society of the Pacific Conference Series*, **314**, 759
- García-Alvarez, D., Foing, B. H., Montes, D., et al. 2002, *A&A*, **397**, 285
- Gehrels, N., Chincarini, G., Giommi, P., et al. 2004, *ApJ*, **611**, 1005
- Giacconi, R., Branduardi, G., Briel, U., et al. 1979, *ApJ*, **230**, 540
- Hall, D. S. 1989, *Space Sci. Rev.*, **50**, 219
- Hall, J. C., Lockwood, G. W., & Skiff, B. A. 2007, *AJ*, **133**, 862
- Hardy, A., Schreiber, M. R., Parsons, S. G., et al. 2015, *ApJ*, **800**, L24
- Huenemoerder, D. P., Mitschang, A., Dewey, D., et al. 2011, *AJ*, **141**, 129
- Jahoda, K., Swank, J. H., Giles, A. B., et al. 1996, in *EUV, X-Ray, and Gamma-Ray Instrumentation for Astronomy VII*, ed. O. H. Siegmund, & M. A. Gummin, *Proc. SPIE*, **2808**, 59
- Jansen, F., Lumb, D., Altieri, B., et al. 2001, *A&A*, **365**, L1
- Jetsu, L., Henry, G. W., & Lehtinen, J. 2017, *ApJ*, **838**, 122
- Kashyap, V., & Drake, J. J. 1999, *ApJ*, **524**, 988
- Lalitha, S., & Schmitt, J. H. M. M. 2013, *A&A*, **559**, A119
- Lanza, A. F. 2005, *MNRAS*, **364**, 238
- Lanza, A. F. 2006, *MNRAS*, **369**, 1773
- Lanza, A. F., & Rodonò, M. 1999, *A&A*, **349**, 887
- Lanza, A. F., Rodonò, M., Mazzola, L., & Messina, S. 2001, *A&A*, **376**, 1011
- Lanza, A. F., Piluso, N., Rodonò, M., Messina, S., & Cutispoto, G. 2006, *A&A*, **455**, 595
- Matsuoka, M., Kawasaki, K., Ueno, S., et al. 2009, *PASJ*, **61**, 999
- Muneer, S., Jayakumar, K., Rosario, M. J., Raveendran, A. V., & Mekkaden, M. V. 2010, *A&A*, **521**, A36
- Osten, R. A., Brown, A., Ayres, T. R., et al. 2004, *ApJS*, **153**, 317
- Paxton, B., Bildsten, L., Dotter, A., et al. 2011, *ApJS*, **192**, 3
- Paxton, B., Cantiello, M., Arras, P., et al. 2013, *ApJS*, **208**, 4
- Pribulla, T., Vaňko, M., Ammler-von Eiff, M., et al. 2012, *Astron. Nachr.*, **333**, 754
- Robrade, J., Schmitt, J. H. M. M., & Favata, F. 2012, *A&A*, **543**, A84
- Rothschild, R., Boldt, E., Holt, S., et al. 1979, *Space Sci. Instrum.*, **4**, 269
- Schleicher, D. R. G., & Mennickent, R. E. 2017, *A&A*, **602**, A109
- Schwabe, M. 1844, *Astron. Nachr.*, **21**, 233
- Soker, N. 2000, *ApJ*, **540**, 436
- Soon, W. H., Baliunas, S. L., & Zhang, Q. 1993, *ApJ*, **414**, L33
- Tanaka, Y., Inoue, H., & Holt, S. S. 1994, *PASJ*, **46**, L37
- Taylor, B. G., Andresen, R. D., Peacock, A., & Zobl, R. 1981, *Space Sci. Rev.*, **30**, 479
- Truemper, J. 1982, *Adv. Space Res.*, **2**, 241
- Tsuboi, Y., Yamazaki, K., Sugawara, Y., et al. 2016, *PASJ*, **68**, 90
- Turner, M. J. L., Thomas, H. D., Patchett, B. E., et al. 1989, *PASJ*, **41**, 345
- van Leeuwen, F. 2007, *A&A*, **474**, 653
- VanderPlas, J. T. 2018, *ApJS*, **236**, 16
- Vaughan, S. 2005, *A&A*, **431**, 391
- Völschow, M., Schleicher, D. R. G., Perdelwitz, V., & Banerjee, R. 2016, *A&A*, **587**, A34
- Wargelin, B. J., Saar, S. H., Pojmański, G., Drake, J. J., & Kashyap, V. L. 2017, *MNRAS*, **464**, 3281
- Warner, B. 1988, *Nature*, **336**, 129
- Weisskopf, M. C., Brinkman, B., Canizares, C., et al. 2002, *PASP*, **114**, 1
- Zechmeister, M., & Kürster, M. 2009, *A&A*, **496**, 577
- Zorotovic, M., & Schreiber, M. R. 2013, *A&A*, **549**, A95

Appendix A

Table A.1. Data resulting from the X-ray analysis.

Instrument	Obs. ID	MJD	Year	$t_{\text{stop}} - t_{\text{start}}$	F_X	ΔF_X	Conversion	χ^2_{red}	Flare?
		d	yyyy.yy	ks	$\frac{10^{-11}\text{erg}}{\text{s.cm}^2}$	$\frac{10^{-11}\text{erg}}{\text{s.cm}^2}$	$\frac{10^{-11}\text{erg}}{\text{s.cm}^2\text{ct}}$		
HEAO1	4U0336+01	43 545.68	1978.10	4.6	1.56	0.23	–	1.10	n
<i>Einstein</i> IPC	I03152	43 900.23	1979.07	19.6	1.92	0.53	0.72	–	–
<i>Einstein</i> SSS	shr1099a	43 904.24	1979.08	0.7	7.65	1.08	–	1.75	y
<i>Einstein</i> SSS	shr1099b	43 905.23	1979.08	0.7	1.69	0.44	–	1.39	n
<i>Einstein</i> IPC	I04496	44 083.59	1979.57	1.6	2.97	0.82	0.72	–	–
<i>Einstein</i> SSS	shr1099c	44 095.70	1979.61	4.4	1.6	0.06	–	3.26	n
<i>Einstein</i> SSS	shr1099d	44 096.22	1979.61	5.3	2.15	0.25	–	1.24	n
<i>Einstein</i> IPC	I02306	44 098.93	1979.62	1.6	2.72	0.75	0.72	–	–
<i>Einstein</i> IPC	I05455	44 277.33	1980.10	4.1	3.33	0.92	0.72	–	–
EXOSAT ME	s10382	45 624.92	1983.79	14.7	7.6	0.13	–	1.12	y
EXOSAT ME	s61328	46 332.39	1985.73	32.8	2.28	0.09	–	1.33	n
EXOSAT ME	s61346	46 332.72	1985.73	8.7	2.52	0.2	–	0.96	n
EXOSAT ME	s70753	46 463.59	1986.09	42.5	1.97	0.08	–	1.69	n
EXOSAT ME	s70792	46 464.08	1986.09	33.8	1.82	0.06	–	0.68	n
EXOSAT ME	s70825	46 464.48	1986.09	29.9	1.63	0.08	–	1.31	n
EXOSAT ME	s70867	46 464.85	1986.09	24.1	1.53	0.05	–	1.52	n
EXOSAT ME	s70893	46 465.17	1986.09	22.6	1.89	0.1	–	0.93	n
Ginga LAC	g880125 232920	47 186.98	1988.07	6.1	5.24	0.36	0.21	–	–
Ginga LAC	g880126 011132	47 187.05	1988.07	233.1	5.01	0.35	0.21	–	–
RASS	RS931710N00	48 102.26	1990.58	0.6	2.92	1.43	0.15	–	–
Ginga LAC	g910823 224507	48 492.95	1991.65	1.1	3.82	0.38	0.21	–	–
ROSAT PSPC	rp200844n00	48 648.44	1992.07	3	1.64	0.80	0.15	–	–
ASCA GIS2	22017000	49 589.16	1994.65	41.9	3.09	0.04	–	1.18	y
ASCA GIS3	22017000	49 589.16	1994.65	41.9	3.12	0.02	–	1.01	y
ASCA SIS0	22017000	49 589.17	1994.65	37.6	3.14	0.07	–	1.08	y
ASCA SIS1	22017000	49 589.17	1994.65	37.7	3.02	0.05	–	1.77	y
ASCA SIS0	22017000	49 589.19	1994.65	24.7	3.29	0.04	–	1.23	y
ASCA SIS1	22017000	49 589.19	1994.65	24.8	3.2	0.06	–	1.33	-
ROSAT HRI	RH202286N00	50 126.43	1996.12	5.4	2.34	0.64	1.13	–	–
ROSAT HRI	RH202288N00	50 126.83	1996.12	5.2	2.69	0.73	1.13	–	–
ROSAT HRI	RH202295N00	50 127.37	1996.12	4.2	3.06	0.83	1.13	–	–
ROSAT HRI	RH202293N00	50 127.76	1996.12	4	3.41	0.93	1.13	–	–
ROSAT HRI	RH202291N00	50 128.31	1996.12	3.9	2.81	0.76	1.13	–	–
ROSAT HRI	RH202290N00	50 128.72	1996.12	3.7	3.92	1.10	1.13	–	–
ROSAT HRI	RH202289N00	50 129.31	1996.13	3.2	3.09	0.84	1.13	–	–
ROSAT HRI	RH202287N00	50 129.65	1996.13	2.2	2.63	0.72	1.13	–	–
ROSAT HRI	RH202292N00	50 130.58	1996.13	1.8	2.96	0.80	1.13	–	–
RXTE PCA	10005010100	50 328.81	1996.67	9.6	2.54	0.11	–	1.29	y
RXTE PCA	10005010101	50 329.75	1996.67	8.9	2.52	0.12	–	1.19	n
RXTE PCA	10005010102	50 330.76	1996.68	8.5	3.44	0.14	–	2.67	y
RXTE PCA	10005010103	50 331.95	1996.68	3.3	4.03	0.19	–	0.83	n
RXTE PCA	10005010104	50 332.01	1996.68	7.8	3.63	0.14	–	1.53	n
<i>BeppoSAX</i> MECS	1045501	51 062.92	1998.68	130.9	1.71	0.04	–	1.15	n
<i>BeppoSAX</i> LECS	1045501	51 062.92	1998.68	62.9	1.45	0.04	–	1.77	n
RXTE PCA	30003010102	51 063.64	1998.68	1.6	1.39	0.08	–	1.13	n

Notes. Column one states the X-ray facility, and, in the case of multi-instrument missions, the instrument. The observing date is given as MJD and year in cols. three and four. The mission-specific Observation ID and duration of the exposure are given in cols. two and five. The resulting X-ray flux and error in the energy range 2–10 keV are given in cols. six and seven. The flux conversion factor (if data is derived from count rates) is given in col. eight, the reduced χ^2 for spectral fits in col. nine and the flare flag in col. ten indicates whether visual inspection of the light curve indicated a major flare during the observation, where “y” denotes an obvious flaring event, “n” stands for no large flare and “–” marks all observations for which a visual inspection was not possible.

Table A.1. continued.

Instrument	Obs. ID	MJD d	Year yyyy.yy	$t_{\text{stop}} - t_{\text{start}}$ ks	F_X $\frac{10^{-11}\text{erg}}{\text{s cm}^2}$	ΔF_X $\frac{10^{-11}\text{erg}}{\text{s cm}^2}$	Conversion $\frac{10^{-11}\text{erg}}{\text{s cm}^2 \text{ ct}}$	χ^2_{red}	Flare?
RXTE PCA	30003010108	51 063.77	1998.68	9.9	2.42	0.13	–	0.71	n
RXTE PCA	30003010100	51 064.71	1998.69	15.9	2.31	0.1	–	1.83	n
RXTE PCA	30003010100	51 065.04	1998.69	1.2	1.86	0.29	–	0.84	n
RXTE PCA	30003010107	51 065.13	1998.69	10	2.15	0.08	–	0.76	n
RXTE PCA	30003010101	51 065.66	1998.69	14.6	2.69	0.19	–	2.13	n
RXTE PCA	30003010101	51 065.97	1998.69	4.4	1.88	9.54	–	1.10	n
RXTE PCA	30003010104	51 066.12	1998.69	3.2	2.06	0.14	–	0.75	n
RXTE PCA	30003010103	51 066.64	1998.69	16	2.67	0.12	–	1.86	n
RXTE PCA	30003010103	51 066.97	1998.69	2.4	1.65	0.24	–	0.75	n
RXTE PCA	30003010106	51 067.00	1998.69	0.8	2.14	0.38	–	0.96	n
RXTE PCA	30003010105	51 067.04	1998.69	7	2.29	0.14	–	0.78	n
<i>Chandra</i> ACIS-S HETG	62538	51 435.95	1999.79	95	4.17	0.05	–	1.00	y
<i>Chandra</i> ACIS-S HETG	1252	51 438.53	1999.80	15	6.31	0.14	–	1.00	n
<i>XMM-Newton</i> PN	0116200701	51 575.39	2000.08	15.1	1.04	0.02	–	1.01	n
<i>XMM-Newton</i> PN	0116340601	51 577.52	2000.09	28.6	1.32	0.02	–	1.17	n
<i>XMM-Newton</i> PN	0116890901	51 582.83	2000.10	40	3.7	0.05	–	1.10	y
<i>XMM-Newton</i> PN	0117890901	51 592.59	2000.13	57.7	2.77	0.02	–	1.00	y
<i>XMM-Newton</i> PN	0129350201	51 784.39	2000.66	31.3	5.96	0.06	–	1.10	y
<i>XMM-Newton</i> PN	0134540101	51 962.75	2001.15	46.3	1.13	0.02	–	1.21	y
<i>XMM-Newton</i> PN	0134540401	52 139.16	2001.63	26.4	1.48	0.02	–	1.05	y
<i>XMM-Newton</i> PN	0134540601	52 508.82	2002.64	35.7	1.15	0.01	–	1.31	y
<i>XMM-Newton</i> MOS1	0134540801	53 230.76	2004.62	51.9	1.71	0.05	–	0.86	y
<i>Swift</i> XRT	50850001	53 352.40	2004.95	0.4	5	0.74	–	1.24	y
<i>Swift</i> XRT	50850002	53 359.23	2004.97	5.3	3.55	0.53	–	1.13	y
<i>Swift</i> XRT	50850008	53 419.04	2005.13	9.1	1.85	0.27	–	1.07	y
<i>Swift</i> XRT	50850009	53 423.05	2005.14	13.9	3.84	0.57	–	0.91	y
<i>Swift</i> XRT	30837001	54 069.87	2006.91	1.9	7.24	1.08	–	1.10	y
MAXI GSC+SSC	—	55 058.52	2009.62	1463	3.9	0.64	–	1.05	y
MAXI GSC+SSC	—	55 788.52	2011.62	1122	5.07	0.52	–	1.06	y
MAXI GSC+SSC	—	56 519.52	2013.62	919.4	4.55	0.67	–	1.05	y
<i>Swift</i> XRT	582894000	56 661.66	2014.01	1	319.22	47.46	–	1.03	y
MAXI GSC+SSC	—	57 249.52	2015.62	933.3	3.64	0.45	–	1.13	y
<i>Swift</i> XRT	88061001	57 833.06	2017.22	3	6.44	0.96	–	0.63	n
<i>Swift</i> XRT	88061002	57 835.00	2017.22	1.6	3.75	0.56	–	1.17	n